공학석사 학위논문

Ionic Diffusion-Driven Ionovoltaic Transducer for Probing Ion-Molecular Interactions at Solid-Liquid Interface

고체-액체 계면에서 이온-분자간 상호작용을 관찰하는 이온 확산 기반의 이온발전소자

2021년 08월

서울대학교 융합과학기술대학원

융합과학부 나노융합전공

한 정 협

Ionic Diffusion-Driven Ionovoltaic Transducer for Probing Ion-Molecular Interactions at Solid-Liquid Interface

지도 교수 김 연 상

이 논문을 공학석사 학위논문으로 제출함
2021년 07월

서울대학교 융합과학기술대학원
융합과학부 나노융합전공
한 정 협

한정협의 공학석사 학위논문을 인준함
2021년 07월

위 원 장 _____ 박 원 철

부위원장 _____ 김 연 상

위 원 _____ 이 강 원

Abstract

Ionic Diffusion-Driven Ionovoltaic Transducer for Probing Ion-Molecular Interactions at Solid-Liquid Interface

Junghyup Han
Program in Nano Science and Technology
Graduate School of Convergence Science and Technology
Seoul National University

Ion-solid surface interactions are one of the fundamental principles in liquid-interfacing devices ranging from various electrochemical systems to electrolyte-driven energy conversion devices. The interplays between these two phases, especially containing charge carriers in the solid layer, are worked as a pivotal role in the operation of these devices. However, corresponding details of those effects remained as unrevealed issues in academic fields. Herein, an ion-charge carrier interaction at an electrolyte-semiconductor interface was interrogated with an ion-dynamics-induced (ionovoltaic) energy transducer, controlled by interfacial self-assembled molecules. An electricity generating mechanism from interfacial ionic diffusion was elucidated in terms of the ion-charge carrier interaction which originated from a dipole potential effect of the self-assembled molecular layer (SAM). In addition, this effect was found to be modulated *via* chemical functionalization

of the interfacial molecular layer and transition metal ion complexation therein. With the aiding of surface analytic techniques and a liquid–interfacing Hall measurement, electrical behaviors of the device depending on the magnitude of the ion–ligand complexation were interrogated, thereby demonstrating the ion–charge carrier interplays spanning at electrolyte–SAM–semiconductor interface. Hence, this system could be applicable to studying molecular interactions, including both chemical and physical influences, occurring at the solid–liquid interfacial region.

Keywords : Electrolyte–semiconductor interface, Ion–charge carrier interaction, Ion–specific adsorption, Ion–ligand complexation, Interfacial potential

Student Number : 2019–21180

Contents

List of Figures

solutions (working solution). 1 M of each ionic solution was tested in the experiment. (d) Normalized current curves as a function of time under 1 M of LiCl, NaCl, and CsCl. A table in Figure 3d denotes a time constant obtained from fitting of each decaying profile.

Figure 4. (a) An equivalent circuit of the transducer. When I_i, an ionic current, is induced by the solution injection, an interfacial charging of ions can attract electrons at a capacitor (C_1), thereby generating electrical currents, I and I_s (electrical currents flow through an external load (R_{ext}) and an internal resistor (R_{sc}), respectively); $R_{sc} = R_1 + R_2 + \cdots + R_n$. After the first interfacial charging at C_1, electrolyte can be diffused in aqueous phase (switch on), and therefore, drive both sequential interfacial charging (C_{n+1}) and dissipation towards bulk phase, simultaneously. R'_{n+1} is an resistance in each ionic diffusion. (b) A simplified equivalent circuit that is considering the first interfacial charging event.

Figure 5. (a,b) Space charge (σ) models of electrolyte–SAM–semiconductor (ESS) interface under (a) high concentration solution and (b) DI water conditions. (c,d) Corresponding vertical potential profiles across the ESS interface under (c) high concentration solution and (d) DI water conditions. Here, the ESS interface can be regarded as a capacitor containing an intrinsic potential difference (ψ_{SAM}), which is derived from the dielectric layer (SAM). σ_{st}, σ_{sc}, and σ_{SAM} are charge density at Stern plane, near the SAM–semiconductor interface, and at SAM interface, respectively. ψ_{sc}, w, and ζ are a potential near the SAM–semiconductor interface, a width of space charge region, and zeta potential, respectively. The subscript ‘s’ and ‘d’ denote an

electrolyte condition of each variable.

Figure 6. (a) A schematic image of ESS interface (PFOTS) with energy band diagram of n-Si near a SAM-semiconductor interfacial region. $\psi_{sc,s} - \psi_{sc,d}$ denotes a difference of potentials under the NaCl solution ($\psi_{sc,s}$) and the DI water ($\psi_{sc,d}$) near the interfacial region in the semiconducting layer. (b) A schematic image of ESS interface (APTES) with energy band diagram of n-Si near a SAM-semiconductor interfacial region.

Figure 7. (a,b) A schematic image of interfacial adsorption-induced electric output variation in the catechol group(CA)-modified ionovoltaic device (CA-IIT) and corresponding interfacial illustrations, which display (a) a pristine state (CA) and (b) Fe^{3+} adsorbed CA state (CA-Fe^{3+}). Dashed lines in Figure 7 (b) denotes coordination bonding between Fe^{3+} and O^- ligands. (c) Generated voltage as a function of time under different $FeCl_3$ concentrations.

Figure 8. (a) Peak voltage and current as a function of exposed $FeCl_3$ concentrations in the catechol group(CA)-modified device (CA-IIT) and Fe^{3+} adsorbed device (Fe-IIT). (b) The pH of $FeCl_3$ solution as a function of concentration. (c) Device resistance as a function of exposed $FeCl_3$ concentrations. Resistances in each condition were obtained from a slope of current-voltage curves, which were measured at both terminals.

Figure 9. (a) C1s XPS spectra of (top) APTES-modified device and (bottom) catechol (CA)-modified device. (b) Fe2p XPS spectra of (top) a pristine CA and (bottom) Fe^{3+} adsorbed surface (CA-

Fe^{3+}) (exposed to 100 μM $FeCl_3$). Dashed lines of A and B denote the peak positions of Fe $2p_{3/2}$ peak obtained from Fe^{2+} with O^- ligands and Fe^{3+} with Cl^- ligands, respectively. (c) Cl 2p XPS spectrum of CA−Fe^{3+} surface (exposed to 100 μM $FeCl_3$).

Figure 10. (a) Hall voltage of the semiconducting layer as a function of magnetic field at the ESS interface. Liquid−interfacing Hall measurements were conducted under (left) DI water and (right) 10 mM NaCl conditions. Constant currents of 5 and 2 μA were applied to catechol group−modified device (CA) (black) and Fe^{3+} adsorbed device (CA−Fe^{3+}) (red). Magnetic field was swept from −105 mT to 105 mT. (b) Normalized carrier density as a function of surface states (CA and CA−Fe^{3+}) under different electrolyte conditions ((left) DI water and (right) 10 mM NaCl).

Figure 11. Relative peak voltage changes as a function of metal ion solution concentrations. Here, V_0 denotes a peak voltage at the pristine (CA−modified) state. According to linear fitting, each slope of $FeCl_3$, $AlCl_3$, and $CuCl_2$ are 3.155, 0.6196, and 0.1052 M^{-1}, respectively.

.

Chapter 1. Introduction

1.1. Study Background

Ion–surface interactions at liquid–solid interfacial boundary are one of the key principles for operating liquid–interfacing devices ranging from electrochemical devices (e.g. battery, electrochemical capacitor) to electronic devices (e.g. bio–/chemical FET sensors and electrolyte–gated synaptic transistors).[1,2] Recently, these interactions also played an important role in water motion–driven electricity generating phenomena.[3,4] As a liquid electrolyte was adjoined with a solid electrode, liquid dynamics–induced collective ionic motions near the interface can trigger unusual electrostatic potential effect in solid electrode, thereby inducing electric current generation in an electrical circuit.[5–10] Detailed origins and process of their ion–surface interactions, which bring about the current flows, are attracting much attention in academic fields.[4,11] Among those effects, an interfacial ion dynamics–driven electricity generating effect, called an ionovoltaic generation, was identified on an electrolyte/dielectric (SAM and insulating layer)/electrode structure.[9,12] This concept was demonstrated in branches of various liquid motions, such as dynamic droplet motions, water evaporation, and capillarity infiltration.[7,9,13–19] Specifically, in terms of driving mechanism, an interfacial dipole effect from orderly deposited molecular layer (self–assembled monolayer, SAM) was proved as a foundation of ion–charge carrier interactions for the electricity generation,[9,12] and was verified by computational simulation results that the intrinsic dipole potential emanating from SAM enables ions adsorbing on SAM to drive simultaneous charging

of compensating charges in electrolyte–SAM (insulator)–semiconductor (ESS) interface. Lately, this was experimentally proved through a liquid–adjoining Hall measurement in ESS structure, which verified that the ion adsorption on SAM can offer a self–gating (without an external gate potential) effect, thereby accumulating charge carriers at the SAM–semiconductor interface.[2,20] These results suggested that, as the semiconductor has a less charge screening capability compared to metallic electrode, it can sensitively vary their charge carrier density near the SAM–semiconductor interface depending on the electrolyte condition.[2,21] Hence, in a same line with various water–motion–induced electricity generating phenomena, ion dynamics in the electrolyte part can induce spatially asymmetric potential in the semiconductor, an electromotive force for the electricity generation.[20] However, understanding and controlling the ionovoltaic effect in semiconducting materials remains imperative since multipronged influences of these dipole potential effects from the electrolyte part to the electrode layer were raised as indispensably investigating area.[16,17,22]

1.2. Purpose of Research

In this study, the interfacial potential effect of surficial molecular layer was investigated in the ESS structure through an ionic diffusion-induced ionovoltaic transducer (IIT). This ionovoltaic measurement in aqueous conditions could be an ideal environment of interrogating the genuine molecular layer effect in the electrolyte-semiconductor interface by excluding subsidiary effects, such as molecular layer degradation under air-exposed condition and triboelectric effect upon sequential solid-liquid contact.[23] An effect of SAM in IIT was informed with both a change of self-assembled molecules, which had opposite dipole potentials, and chemical adsorption of transition metal ion in chemically functionalized SAM.[16,17] Corresponding intrinsic potential effect of the molecular layer, affecting to the semiconductor, was investigated with various surface analytic techniques. Interfacial interplays across the ESS structure were analyzed with a liquid-interfacing Hall measurement, and therefore, ion-chelating on molecular layer was revealed to modulate electrical characteristics at the SAM-semiconductor interface by the intrinsic potential modulation of the molecular layer. This was correlated with the output signal behaviors in IIT upon ion-chelating process. Ion-chelating-dependent output signal variation in IIT shows a strong potential toward interfacial adsorption-induced probing devices, such as chemical sensing and interfacial analytic tools.

Chapter 2. Experimental Section

2.1. Device fabrication

Silicon (Si) wafer (n-type, 1000Ω·cm, 525 ± 15 μm, MTI Corporation) was cut into 0.8 x 7 cm^2 and ultrasonicated sequentially with detergent, DI water, acetone, and isopropyl alcohol (IPA) for 15 min each. O_2 plasma (0.6 torr, 100W) was treated on the Si substrate for 30 s to form silanol groups (Si-OH) for the deposition of a self-assembled monolayer (SAM) on a native SiO_2. Experimental processes of surface modification with two different SAMs are presented in Figure 1a. 1H,1H,2H,2H-perfluorooctyltrichlorosilane (PFOTS) was deposited by chemical vapor deposition. The O_2 plasma-treated Si was placed in a desiccator with a slide glass containing 30 μL PFOTS under vacuum for 10 min at room temperature. The PFOTS-treated Si was rinsed with IPA and annealed at 120 ℃ for 20 min to remove untreated PFOTS. The PFOTS-modified device (P-IIT) was prepared. (3-aminopropyl)triethoxysilane (APTES) was deposited by liquid phase dipping. The O_2 plasma-treated Si was dipped in 2 % (v/v) APTES in toluene at 90 ℃ for 1 hr. The APTES-treated Si was sonicated with toluene for 1 min, rinsed with toluene and ethanol sequentially, and dried under N_2 flow. The APTES-modified device (A-IIT) was prepared. Additional surface modification on A-IIT to graft catechol groups (CA) was conducted. At first, dihydrocaffeic acid (DHCA) was conjugated with NHS (N-Hydroxysuccinimide) as shown in Figure 1b. DHCA, EDC·HCl (1-(3-Dimethylaminopropyl)-3-ethylcarbodiimide Hydrochloride),

and NHS were mixed in a 0.1 M MES (2-(N-Morpholino)ethanesulfonic acid hydrate) aqueous solution, and their final concentrations were 20 mM, 80 mM, and 40 mM, respectively. DHCA was activated to NHS-conjugated DHCA (NHS-DHCA) for 15 minutes. Then, the A-IIT was dipped in the NHS-DHCA solution for 1hr and rinsed with DI water. The CA-modified device (CA-IIT) was prepared, and it was exposed to $FeCl_{3(aq)}$ solution for 10 minutes to prepare Fe^{3+} adsorbed device (Fe-IIT) as presented in Figure 1c.

2.2. Characterizations

Chemical states of the devices (P-IIT, A-IIT, CA-IIT, Fe-IIT) were characterized by X-ray photoelectron spectroscopy (XPS, NEXSA, ThermoFisher Scientific). To characterize potential difference at the SAM, Ultraviolet photoelectron spectroscopy (UPS, NEXSA, ThermoFisher Scientific) were conducted. The work function of each device was obtained, and its shift referred to bare-Si was calculated. To characterize a potential above the surface, surface zeta potential measurement (SurPASS^{TM}3, Anton Paar) was performed under DI water and a 10 mM NaCl solution. The samples measured in XPS, UPS, and surface zeta potential were prepared in the same manner with the preparation of the devices. For the electrical characterization of the devices, both lateral ends of the exposed Si electrode of the prepared device were connected to the wire and sealed with an epoxy resin to prevent leak current when in contact with water. Then, the device was placed on the center of a round Petri dish bath, and 35 mL of DI water was filled into the bath to soak the device. A Keithley 2182A nanovoltmeter and 6485

picoammeter were used to measure output voltage and current, respectively. The probe of the electrical measurement unit was connected to the wire near where an ionic solution will be injected, and the ground electrode was connected to the other wire. A micropipette tip filled with 5 M $NaCl_{(aq)}$ 50 μL was vertically brought above the one end of the device connected with the probe to contact DI water in the bath using a custom-built tensile strength tester. Then, the electrical outputs were generated. A liquid-interfacing Hall measurement was conducted to characterize the carrier density of the silicon electrode. Four terminals at the centers of each edge of the exposed Si electrode of the fabricated CA-IIT and Fe-IIT (1.0 x 1.0 cm^2) were connected to wires and sealed with an epoxy resin. The current line and the voltage line were cross-connected, and the samples were put into a 15 mL conical tube with 4 mL of DI water and 10 mM NaCl to completely soaked, respectively. While applying an external magnetic field in the direction on the vertical plane of the sample, the current, 5 μA and 2 μA was constantly applied to the current line on CA-IIT and Fe-IIT, respectively. Then, the Hall voltage with the sweeping magnetic field from −105 mT to 105 mT was measured with Keithley 197 Auto-ranging microvolt DMM, and the frequency of the function generator was set to 1.7mHz. The number density of charge carriers in the semiconductor was calculated by the definition of the Hall effects and normalized to compare that in CA-IIT and Fe-IIT.

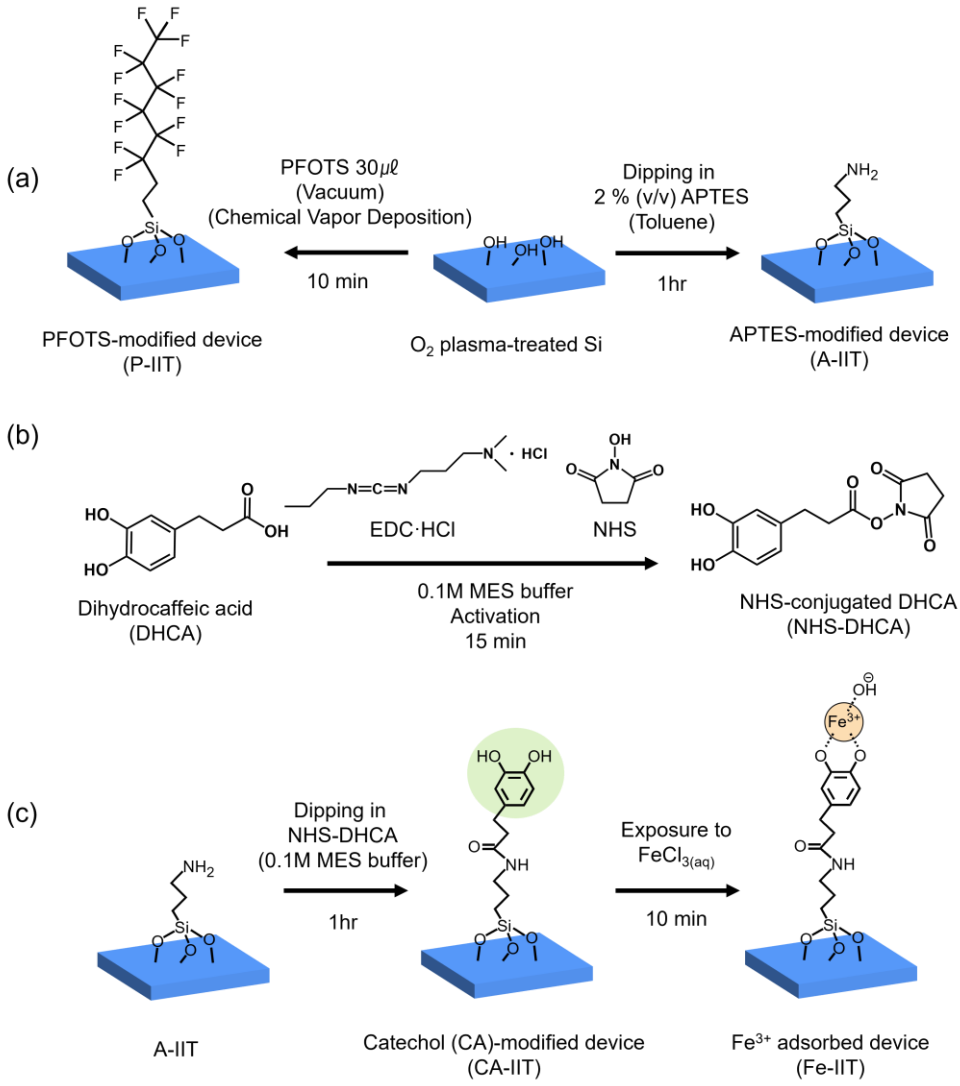

Figure 1. Experimental process for device fabrication. (a) Surface modification to fabricate P-IIT and A-IIT by PFOTS and APTES deposition on the O_2 plasma-treated Si, respectively. (b) Activation of DHCA by mixing with EDC·HCl and NHS in MES aqueous solution. (c) Surface functionalization of A-IIT by NHS ester reaction to produce CA-IIT, and exposure of CA-IIT to $FeCl_{3(aq)}$ solution to prepare Fe-IIT.

Chapter 3. Results and Discussion

3.1. Investigation on IIT

Figure 2a shows a schematic image of electric signal transduction by an electrolyte effect on P-IIT. As the highly concentrated ions diffuse out, cations adsorb in an electrical double layer (EDL) due to the negative surface potential of PFOTS, and this adsorption process can be propagated in a lateral direction.[24] In this situation, electrons in the semiconducting layer can be attracted toward the SAM-semiconductor interface by an intrinsic dipole potential of molecular layer, and consistently with ionic process, this accumulation could be propagated in the lateral direction at the SAM-semiconductor interface.[9,20] Hence, electrical outputs could be induced in P-IIT as shown in Figure 2b. At first, the generated current and voltage were abruptly evolved and reached an apex, and then they gradually decayed. This could be correlated with the ionic diffusion process at the electrolyte-SAM interface. In this experiment, the highest value was used to explain electric outputs where the effect of the ionovoltaic generation driven by an ionic diffusion is maximized. Since using the electrical signal of peak value is appropriate for a brief explanation, the experimental results will be interpreted based on the maximum value, and 50 μL of 5 M NaCl solution is set as a working solution. For a better understanding of the energy generation in IIT, influences of molecular layer were further investigated with changing components of the system. Instead of PFOTS, (3-aminopropyl)triethoxysilane (APTES) was treated on IIT, and the

corresponding device (A−IIT) outputs were measured under the same condition of P−IIT. As shown in Figure 2b, the peak voltage and peak current were 21.6 mV and 21.9 nA in P−IIT. As compared to them, similar but reversed voltage and current profiles were measured in A−IIT, and those had maximum peaks of −11.84 mV and −9.35 nA, respectively. This could be due to the reversed surface charge and molecular dipole of APTES against PFOTS. According to Figure 2c, the surface potential of APTES is positive and thereby inducing an anion adsorption in EDL.[25] The dipole potential effect of APTES was also opposite to that of PFOTS as shown in Figure 2d (UPS).[26,27] This can indicate that, as a similar process with the cation−electron interplays in the PFOTS−containing ESS structure, the anion adsorption at APTES could expel electrons (or attract holes) at the SAM−semiconductor interface. This could be an origin of the reversed electrical outputs on A−IIT. Next, an influence of the Si electrode dimension was also interrogated with P−IIT. The electrical measurements on the device were conducted with different widths and lengths, as shown in Figure 3a. At the device with fixed width (w = 0.8 cm), the peak voltage increased linearly (6.7 to 22.5 mV) with increasing length (l = 2 to 6.4 cm), and there were negligible changes in peak current (from 20.5 to 22.7 nA). On the contrary, the linear increases of the peak current from 20.1 to 32.9 nA were observed with increasing width from 0.8 to 1.6 cm at the device with fixed length (6.4 cm) but peak voltage had little change (from 19.8 to 17.8 mV). To elucidate the electrical behaviors of of P−IIT, resistances of each condition were measured as presented in Figure 3b. Under the fixed w (= 0.8 cm), the device resistances were increased linearly from 0.368 to 0.806 MΩ with elongating l from 2 to 6.4 cm. On the other

hand, under the fixed l (= 6.4 cm), the resistance decreased inversely with rising w from 0.864 (w = 0.8 cm) to 0.326 MΩ (w =1.6 cm). Lastly, as mentioned in Figure 2a, electricity generation induced by the ionic diffusion process at the electrolyte−SAM interface was interrogated under different cation conditions (1 M of LiCl, NaCl, KCl, and CsCl). As shown in Figure 3c, Cs^+ achieved a highest current, 10.5 nA, among all cations, and these peak values had an order as follows; $Cs^+ > K^+ > Na^+ > Li^+$. In addition, Cs^+ also reached the peak value in the shortest time, 385 ms, and rapidly decayed as compared to other ions, as presented in Figure 3d. This upsurge and attenuation times were also consistent as follows; $Cs^+ > K^+ > Na^+ > Li^+$. All these results are matched with an order of ionic diffusivities ($Cs^+ > K^+ > Na^+ > Li^+$),[28] indicating that the electric signal generation in IIT has a dependence on the ionic diffusion process at the electrolyte−SAM interface. And, as abovementioned, the ion adsorption in EDL can propagate laterally at the electrolyte−SAM interface by the ionic diffusion, thereby inducing charge carrier movements at the SAM−semiconductor interface (Figure 2a). This ESS interface can be regarded as a multi−capacitor model,[3,5,9] and details of the corresponding interpretation were explained in Figure 4 and Figure 5. An equivalent circuit of IIT with capacitor model was suggested in Figure 4, and the equation of the device output was derived. When P−IIT with certain width (w) and length (l) was immersed in DI water, charging of cations at the PFOTS−electrolyte interface can be induced by the diffusion process (Aqueous phase in Figure 4a). This interfacial charging is driven by an intrinsic potential difference emanating from PFOTS, and therefore, it is reasonable to regard ESS interface as a unit capacitor (from C_1 to C_n) at each

area.[3,5,9] Hence, the same number of electrons, equivalent to an amount of the adsorbed ions, can be accumulated at the PFOTS–semiconductor interface. In the circuit of Figure 4a, $R'_1 \sim R'_n$ and $R_1 \sim R_{n-1}$ represents resistance of a unit resistor in aqueous phase and in semiconductor, respectively, between each capacitor, and $R_1 + R_2 + \cdots + R_{n-1} = R_{sc}$, which is a resistance of the semiconductor near the SAM–semiconductor interface. After an injection of highly concentrated solution, an ionic current (I_i) by the interfacial ion charging (at C_1) can drive an equal amount of electrical current in the semiconductor ($I + I_s$, where I and I_s are electrical currents flowing through an external load and the semiconductor, respectively). Sequentially, lateral diffusion process (serial switch on in Figure 4a) enables the concentrated ions to be charged at C_n or dissipated toward bulk part, thereby inducing both equivalent charging of electrons at C_n and corresponding electrical current (I and I_s) at the electronic circuit. However, as compared to the first interfacial charging (at C_1), which is driven by the diffusion under an initial concentration of the electrolyte, the amount of adsorbed ions at the posterior capacitors (from C_2 to C_n) could become reduced due to an ion dissipation toward a bulk part. Hence, as shown in Figure 2b, the electric output could have an apex at the first charging (C_1) and then be decayed as time goes by. Herein, the apparent peak of electric outputs is considered as a major signal, and a corresponding simplified equivalent circuit is displayed at Figure 4b. In the circuit, a relation between each current flow can be expressed by

(E1) $I = I_i - I_s$

Voltage measured in external voltammeter (V) can be presented as follows;

(E2) $V = I_s R_{sc} - I R_{ext}$

, where R_{ext} is a resistance in external circuit including contact resistances and assumed to be much smaller than R_{sc}. I_i by the solution injection can be expressed with dQ/dt, where Q is an amount of ions (electrons) adsorbed (accumulated) at the electrolyte−SAM−semiconductor interface. Hence,

(E3) $I_i = \frac{dC_1}{dt}\Delta\psi$

, and $\Delta\psi$ is a potential difference between electrolyte and semiconductor, which are in the vicinity of the SAM interface. This is equivalent to a potential difference between underneath the ion−adsorbed interface (denoted with subscript 's') and un−adsorbed (DI water) interface (denoted with subscript 'd') in the semiconducting layer. Hence, the equation (E1) can be denoted with both the equation (E2) and the equation (E3) as follows;

(E4) $I = -\frac{1}{R_{sc}}\left(V - R_{sc}\frac{dC_1}{dt}\left(\psi_{sc,s} - \psi_{sc,d}\right)\right)$

$\psi_{sc,s}$ and $\psi_{sc,d}$ denote a potential of semiconductor near the SAM interface under the ion−adsorbed region and un−adsorbed region, respectively. Due to the diffusion−induced capacitive charging (Figure 2a), $\frac{dC_1}{dt}$ can be expressed with an adsorption speed in electric double layer (D/λ_D, where D and λ_D are a diffusion coefficient of adsorbed ion and Debye length, respectively) as follows;[29]

(E5) $\frac{dC_1}{dt} = \frac{D}{\lambda_D}\varepsilon_0\varepsilon_{SAM}\frac{w}{d}$

Herein, ε_0, ε_{SAM}, and d are vacuum permittivity, relative permittivity of SAM, and a thickness of SAM, respectively. λ_D is assumed as DI water condition (equivalent to an initial state in the experiment). Thus, the equation (E4) can be expressed as follows;

(E6) $I = -\frac{1}{R_{sc}}\left(V - R_{sc}\frac{D}{\lambda_D}\varepsilon_0\varepsilon_{SAM}\frac{w}{d}\left(\psi_{sc,s} - \psi_{sc,d}\right)\right)$

In a short-circuited condition, V=0, and then

(E7) $I_p = \frac{D}{\lambda_D}\varepsilon_0\varepsilon_{SAM}\frac{w}{d}\left(\psi_{sc,s} - \psi_{sc,d}\right)$

In an open-circuited condition, I=0, and then

(E8) $V_p = R_{sc}\frac{D}{\lambda_D}\varepsilon_0\varepsilon_{SAM}\frac{w}{d}\left(\psi_{sc,s} - \psi_{sc,d}\right)$

, which is equivalent to $V_p = I_p \times R_{sc}$. The equation (E8) can be expressed with a sheet resistance of semiconductor (R_{sq}) by considering the extrinsic factors as follows.

(E9) $V_p = R_{sq}\, l\frac{D}{\lambda_D}\frac{\varepsilon_0\varepsilon_{SAM}}{d}\left(\psi_{sc,s} - \psi_{sc,d}\right)$

In the equation (E7), $\psi_{sc,s} - \psi_{sc,d}$ is a driving force of charge carrier flows near the SAM-semiconductor interface. As assumed before, the electrolyte-SAM-semiconductor interface can be regarded as the capacitor, of which electrodes have different potential screening capabilities. As shown in Figure 5a and 5b, an equal quantity of charges (ions and electrons) can be accumulated at the SAM (PFOTS) interface, which can have an interfacial charge density of σ_{SAM}. Hence, in both high (subscript 's') and low (subscript 'd') concentration regions, an adsorbed ion density at Stern layer ($\sigma_{st,s}$ and $\sigma_{st,d}$, respectively) can be equivalent to the charge density (per unit area) at the SAM-semiconductor interface ($\sigma_{sc,s}$ and $\sigma_{sc,d}$, respectively) ($\sigma_{st} = \sigma_{sc}$). As σ_{sc} can be expressed as

(E10) $\sigma_{sc} = qNW$

, where q, N, and W are an electron charge, a dopant density, and a width of space charge region, respectively.[30] qN is constant throughout the semiconducting layer. From the zeta potential (ζ) measurement, $\zeta_s < \zeta_d$ indicated that $\sigma_{st,s} > \sigma_{st,d}$ (Figure 2c). Hence, in the high concentration region, larger $\sigma_{sc,s}$ than $\sigma_{sc,d}$ can induce a

relatively wider W_s than W_d (Figure 5a and 5b). ψ_{sc} can be shown with σ_{sc} and W as follows;[30]

(E11) $\psi_{sc} = -\frac{\sigma_{sc} W}{2\varepsilon_0 \varepsilon_{sc}}$

ε_{sc} is a dielectric constant of the semiconductor. Hence, as shown in Figure 5c and 5d, $\psi_{sc,s}$ can be much larger than $\psi_{sc,d}$ and spanned to deeper region in the semiconductor. Therefore, in the PFOTS case, $\psi_{sc,s} > \psi_{sc,d}$ and this was consistent with the current direction in Figure 2b. On the other hand, in the case of APTES, the anion adsorption at the electrolyte−SAM interface could induce repulsion of electrons (or accumulation of holes) at the highly concentrated region due to its opposite dipole from PFOTS (Figure 2d), thereby driving reversed potential direction in semiconducting layer underneath the SAM interface. Hence, A−IIT can have a reversed pole in its output signals as shown in Figure 2b. Among those process, the highest peak values of electrical outputs were considered, and corresponding equations of peak current (I_p) and voltage (V_p) were expressed as follows;

(E12) $I_p = \frac{D}{\lambda_D} \varepsilon_0 \varepsilon_{SAM} \frac{w}{d} (\psi_{sc,s} - \psi_{sc,d})$

(E13) $V_p = R_{sc} I_p$

As discussed in Figure 3c and 3d, alkali ion species−dependent I_p was consistent with a direct correlation between I_p and $\boldsymbol{D}$, indicating that the transient ionic motions at the ESS interface enabled to flow the charge carriers in semiconducting layer, and naturally, this concentrated ion propagation near EDL could induce a driving potential, $\psi_{sc,s} - \psi_{sc,d}$ (a potential difference between highly concentrated and DI water regions), for the charge carrier flows in the semiconducting layer. As shown in Figure 2c and 2d, PFOTS had the negative zeta potentials, relying on the electrolyte

concentration, and the interfacial dipole potential whose negative pole was positioned at surface.[24] Hence, $\psi_{sc,s} - \psi_{sc,d}$ of PFOTS containing ESS interface was theoretically analyzed as discussed in Figure 5, and therefore, $\psi_{sc,s}$ could be higher than $\psi_{sc,d}$. Eventually, the transition from the DI water–contacted state to the highly concentrated ion condition at EDL can trigger a shift of energy of charge carriers underneath the SAM–semiconductor interface (from red to blue in Figure 6a), thereby inducing an electric current flow in an external circuit. As APTES has opposite surface charges and dipole potentials (Figure 2c and 2d), A–IIT could have a reversed driving potential as compared to P–IIT. Hence the diametrical electric outputs can be generated by the opposite carrier motions in the semiconducting layer (Figure 2b and Figure 6b). The electrical outputs of IIT can also be affected by the device resistance, which can be correlated to the device dimension (Figure 3a and 3b). As shown in the equation (E12), I_p has a direction correlation with w, whereas V_p can have a direct correlation with l as shown in the equation (E9), a reduced form of the equation (E13). These results were consistent with Figure 3a. Interestingly, those results also indicated that R_{sc} could be a determining factor for V_p, and V_p of IIT could relies on a voltage drop effect in the semiconducting layer adjoining the SAM interface.[9,19]

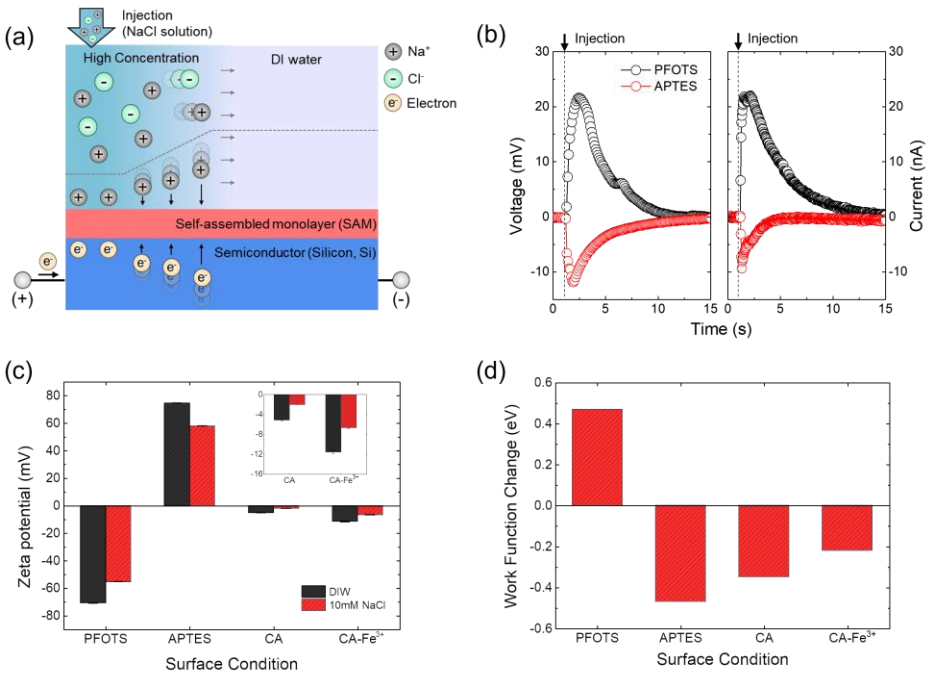

Figure 2. (a) A schematic image of ionic diffusion-induced electricity generation at electrolyte-SAM-semiconductor (ESS) interface. In the experiments, a highly concentrated solution (NaCl 5 M, 50 μL) was injected into DI water bath (35 mL). N-type silicon was utilized as a semiconducting layer in the experiments. (b) Generated voltage and current as a function of time under difference SAM conditions (PFOTS and APTES). The NaCl solution, which is a working solution in this experiment, was injected into water bath at ~1 s. (c) Zeta potential (ζ) under different surface conditions. (d) Work Function changes of Si under different surface conditions. Each measured value was subtracted with a work function of bare Si as a reference (3.23 eV).

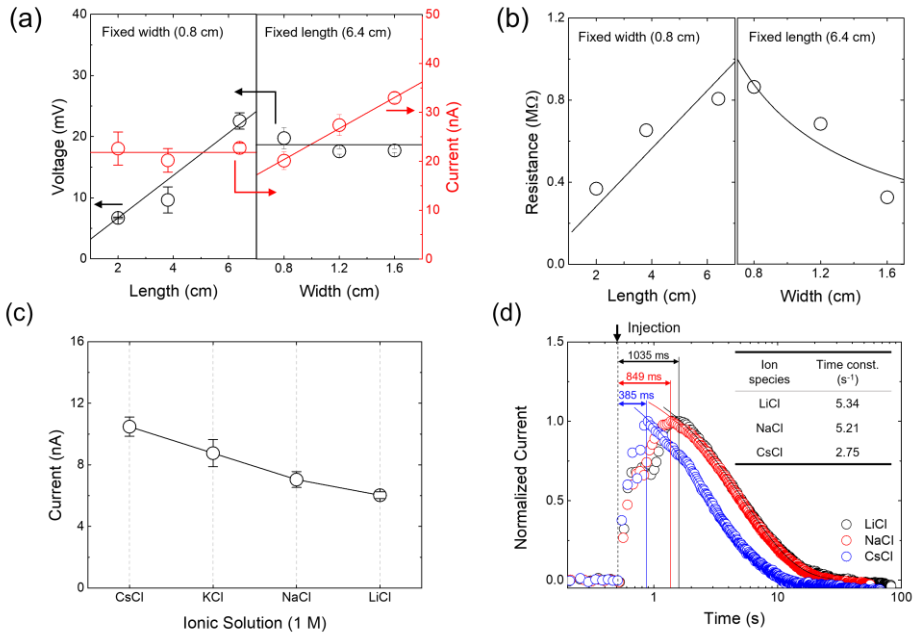

Figure 3. (a) Generated peak voltage and current as a function of device length (l, left) and width (w, right). In the l−dependent output measurement, w was fixed with 0.8 cm. In the w−dependent output measurement, l was fixed with 6.4 cm. (b) Measured resistance as a function of device dimensions ((left) length and (right) width) (c) Generated peak current under different alkali ion solutions (working solution). 1 M of each ionic solution was tested in the experiment. (d) Normalized current curves as a function of time under 1 M of LiCl, NaCl, and CsCl. A table in Figure 3d denotes a time constant obtained from fitting of each decaying profile.

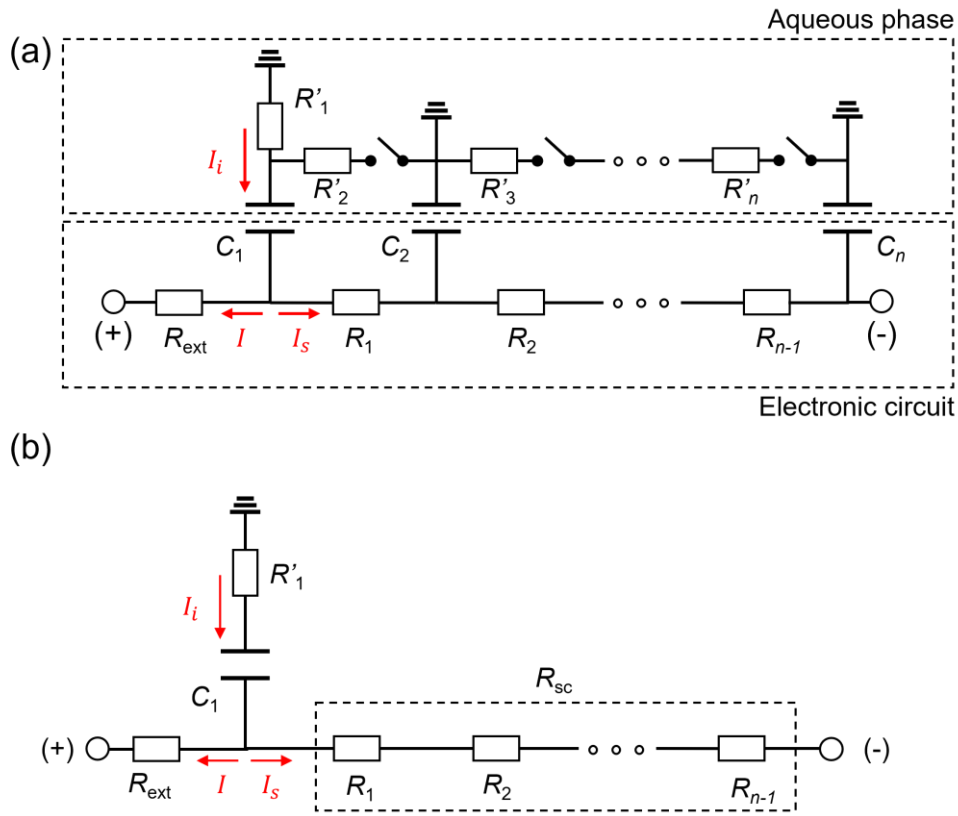

Figure 4. (a) An equivalent circuit of the transducer. When I_i, an ionic current, is induced by the solution injection, an interfacial charging of ions can attract electrons at a capacitor (C_1), thereby generating electrical currents, I and I_s (electrical currents flow through an external load (R_{ext}) and an internal resistor (R_{sc}), respectively); $R_{sc} = R_1 + R_2 + \cdots + R_n$. After the first interfacial charging at C_1, electrolyte can be diffused in aqueous phase (switch on), and therefore, drive both sequential interfacial charging (C_{n+1}) and dissipation towards bulk phase, simultaneously. R'_{n+1} is an resistance in each ionic diffusion. (b) A simplified equivalent circuit that is considering the first interfacial charging event.

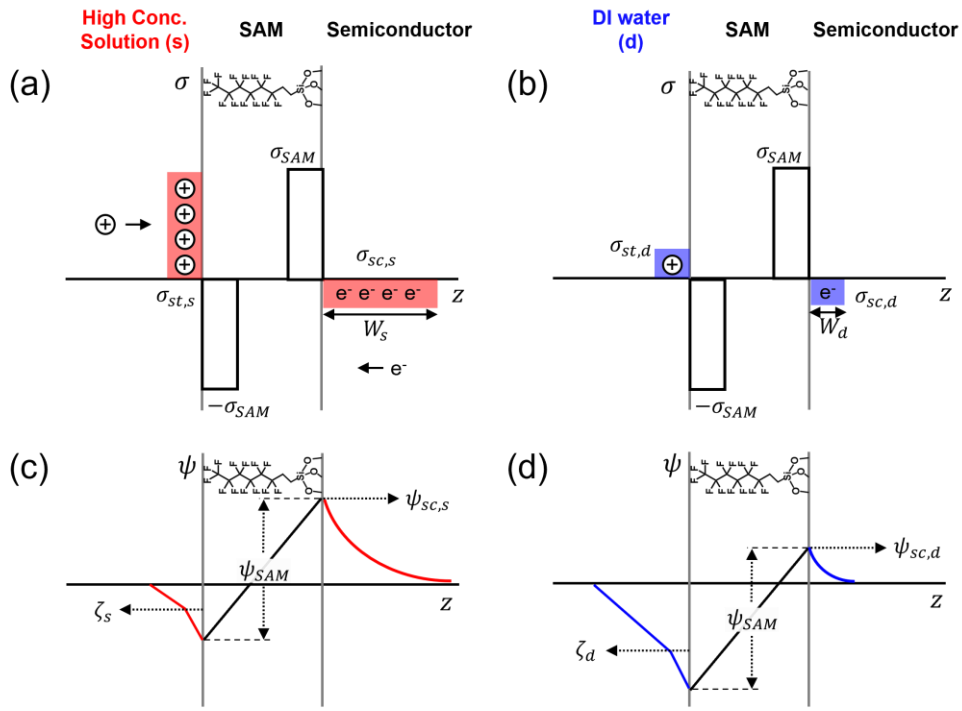

Figure 5. (a,b) Space charge (σ) models of electrolyte–SAM–semiconductor (ESS) interface under (a) high concentration solution and (b) DI water conditions. (c,d) Corresponding vertical potential profiles across the ESS interface under (c) high concentration solution and (d) DI water conditions. Here, the ESS interface can be regarded as a capacitor containing an intrinsic potential difference (ψ_{SAM}), which is derived from the dielectric layer (SAM). σ_{st}, σ_{sc}, and σ_{SAM} are charge density at Stern plane, near the SAM–semiconductor interface, and at SAM interface, respectively. ψ_{sc}, w, and ζ are a potential near the SAM–semiconductor interface, a width of space charge region, and zeta potential, respectively. The subscript 's' and 'd' denote an electrolyte condition of each variable.

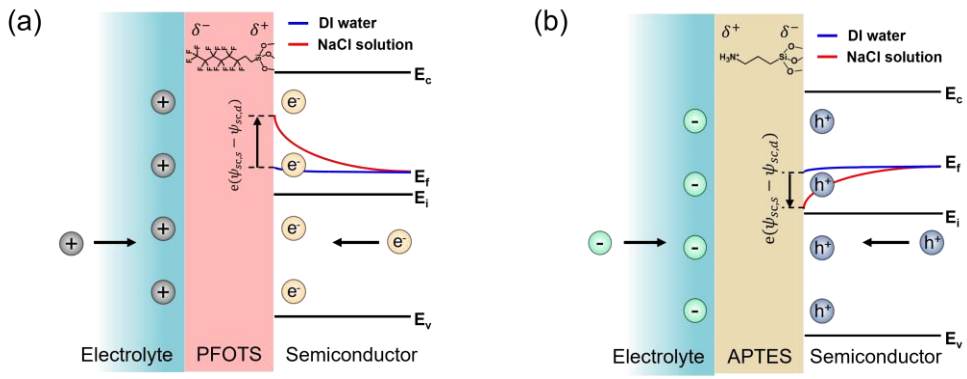

Figure 6. (a) A schematic image of ESS interface (PFOTS) with energy band diagram of n−Si near a SAM−semiconductor interfacial region. $\psi_{sc,s} - \psi_{sc,d}$ denotes a difference of potentials under the NaCl solution ($\psi_{sc,s}$) and the DI water ($\psi_{sc,d}$) near the interfacial region in the semiconducting layer. (b) A schematic image of ESS interface (APTES) with energy band diagram of n−Si near a SAM−semiconductor interfacial region.

3.2. Effects of the ion-specific adsorption at the electrolyte-SAM-semiconductor interface

To investigate the interfacial molecular effect by an ion-specific adsorption in ESS structure, ion-chelating ligand group was introduced at the ESS structure. Catechol group (CA), which can form a coordination complex with various metal ions, and especially stable with ferric ions (Fe^{3+}),[31,32] was adopted *via* a chemical modification of APTES as follows; dihydrocaffeic acid (DHCA), which has CA and carboxylic group, was activated by 1-(3-dimethylaminopropyl)-3-ethylcarbodiimide hydrochloride (EDC · HCl) and N-hydroxysuccinimide (NHS) to form NHS-conjugated DHCA (NHS-DHCA), and then A-IIT was treated with NHS-DHCA as shown in Figure 1. A corresponding schematic image of CA-modified SAM and its electrical output in CA-IIT were shown in Figure 7a and 7c. The prepared CA-IIT generated V_p of ~3.3 mV and its time-dependent profile was similar and equivalently polarized with that from P-IIT. Under the same diffusion process with P-IIT, this reduced electrical output in CA-IIT could be originated from a heterogeneous CA-modified surface, containing both remaining amine group from APTES and hydroxyl moieties from CA (Figure 7a). After the CA functionalization, the surface zeta-potential was shifted from highly positive values (Figure 2c, 74.6 and 57.9 mV at DI water and 10 mM conditions, respectively) to slightly negative regions (Figure 2c, -5.12 and -1.99 mV at DI water and 10 mM conditions, respectively) due to an influence of hydroxyl group in CA.[33] To investigate an effect of the Fe^{3+}-CA complexation in SAM to IIT, the generated voltage variation upon exposures of $FeCl_3$ solution (from 10^{-7} to 10^{-2} M)

was monitored as shown in Figure 7c and Figure 8a. As the exposed solution concentration increased, a magnitude of the generated voltages in the Fe^{3+} adsorbed device (Fe−IIT) was elevated up to ~9.6 mV (10^{-3} M) with presenting similar time−dependent profiles. This indicated that the uniform ion dynamics were applied to operate IITs, and the voltage shifts could be derived from changes of the ion−charge carrier interactions by the Fe^{3+}−CA complexation in SAM. Figure 8a displayed both V_p and I_p of IITs under different $FeCl_3$ concentrations. Consistently with Figure 7c, V_p was increased in a range of 10^{-7}−10^{-3} M and saturated at 10^{-2} M, but I_p showed a little increase in that range (from 5.36 nA at pristine state to 6.17 nA at 10^{-3} M). The saturation of V_p over 10^{-3} M could be induced from the low pH at this concentration range (Figure 8b), which can interrupt the Fe^{3+}−CA complexation.[34] As displayed in the equation (E13), V_p relies on two factors, R_{sc}, the resistance of the semiconducting layer near the SAM interface, and I_p. Chemical interactions between CA and Fe^{3+} can rely on surrounding environments, such as pH and their relative quantity of them. In this experimental condition, Fe^{3+} could favorably form a mono−complex with surface−grafted CA due to our pH condition, less than 6 (Figure 8b),[34] and a steric effect between them.[35] In high $FeCl_3$ concentrations (over 10^{-3} M), low pHs can hamper the Fe^{3+}−CA complexation because the hydroxyl group on CA can preferably exist in a −OH form not in a $-O^-$ form, which is favorable for the Fe^{3+} complexation. Simultaneously with this, the CA complexed Fe^{3+} could interact with negative hydroxide ions (OH^-) due to the strong acidity of Fe^{3+}, thereby binding with them in the aqueous interface (Figure 7b).[36,37] Hence, the Fe^{3+} complexed SAM showed more negative zeta potential than does not

(Figure 2c), and due to this, more cations can be attracted to the electrolyte–SAM interface than pristine CA surface. This effect could induce a higher driving potential ($\psi_{sc,s} - \psi_{sc,d}$) at Fe–IIT than CA–IIT, thereby contributing to the slightly increased I_p depending on the Fe^{3+} complexation (Figure 8a). However, the experimental results in Figure 8a implied that, as compared to I_p, the drastic V_p shifts could be majorly originated from a change of R_{sc} upon the Fe^{3+}–CA complexation in SAM. This could be supported by a gradual elevation of the bulk resistance of the semiconductor by the interfacial Fe^{3+} complexation (Figure 8c, from 1.15 (pristine) to 1.23 (10^{-2} M) MΩ). Hence, this indicated that the Fe^{3+}–CA complexation in SAM also could critically influence to the semiconducting layer adjoining the SAM interface. In our previous work, the ionovoltaic generation was confirmed to be regulated by modulations of interfacial molecular layer (e.g. ion adsorption and molecular interaction).[16,17] In these works, physicochemical interactions of the interfacial molecular layer were monitored *via* an electrolyte–SAM–metallic electrode interface, and the interfacial molecular dipole effect genuinely determined the electrical behaviors in the device. However, those results indicated that the Fe^{3+}–CA complexation in SAM significantly influenced both the electrolyte and the semiconducting layer, thereby inducing complicated electrical behaviors (increasing V_p and constant I_p) in the IIT. To identify a dominant factor for the electrical behavior by Fe^{3+}–CA complexation, X–ray photoemission spectroscopy (XPS) analysis and a liquid–interfacing Hall measurement were conducted in Figure 9 and Figure 10, respectively. The chemical composition of each surface was identified through XPS analysis. Figure 9a showed C1s spectra of both APTES–modified (top) and catechol

group-functionalized (bottom) surfaces. C1s spectrum showed peaks from APTES derivatives, amine group (C-N, 286.0 eV) and aliphatic carbon chains (C-C, ~284 eV).[38] However, a peak of amide bond (N-C=O, 288.0 eV), which was absent in APTES-treated surface, was evolved after EDC/NHS reaction as presented in CA-modified surface, indicating that catechol groups had successfully grafted to the surface. To investigate the chemical states of coordination complex, XP spectra of Fe2p at the CA-modified (top) and Fe^{3+} adsorbed surfaces (CA-Fe^{3+}, bottom) were shown in Figure 9b. The characteristic doublet peaks of $Fe2p_{3/2}$ and $Fe2p_{1/2}$, which were not exhibited at the CA, were evolved at the CA-Fe^{3+} showing the presence of iron elements on the surface. As shown in Figure 9b, a binding energy of $Fe2p_{3/2}$ peak (711.1 eV) at the CA-Fe^{3+} was positioned between A, ferrous ionic state (Fe^{2+}) (709.0 eV, Fe_2SiO_4),[39] and B, ferric ionic state (Fe^{3+}) (711.5eV, $FeCl_3$).[40] This indicated that the chemical state of CA-Fe^{3+} could be an oxygen group coordinating state, offered by CA, instead of counter-anion (Cl^-). Iron ion in the solution of $FeCl_3 \cdot 6H_2O$ mainly exists in the form of $[Fe(H_2O)_4Cl_2]^+$, which has two Cl^- ligands.[41,42] During the Fe^{3+}-CA complexation, Cl^- ligands of iron ion are exchanged to O^- ligands from CA. This was supported by a XPS spectrum of Cl2p at the Fe^{3+}-CA where no peak was evolved (Figure 9c). According to the crystal field theory, $-O^-$ group is stronger field ligand than $-Cl^-$ and then forms a large splitting of d-orbitals in a coordination complex in which the outermost electrons of Fe^{3+} could be mostly in orbitals at t_{2g} level that is lower than e_g level.[43,44] Therefore, the binding energy of Fe^{3+} with $-O^-$ ligands can be smaller than that with Cl^- because electron might be easily eliminated in a lower spin complex with $-O^-$ ligands. To

investigate the influence of the Fe^{3+}−CA complexation to the SAM−semiconductor interface, a liquid−interfacing Hall measurement was conducted as presented in Figure 10. This measurement is a novel analysis to interrogate the ion−semiconductor interaction at the solid−liquid interface.[20] The measurements were conducted on the CA−IIT and Fe−IIT submerged in DI water and 10 mM NaCl solution, and optimal biasing currents were applied for each device due to their different resistances (CA : 5 μA, CA−Fe^{3+} : 2 μA, experimental section). Hall voltage (V_H) was measured by applying an external magnetic field in a normal direction to the sample surface (−105 to 105 mT), and slopes were calculated by linear regression in Figure 10a. Then, the number density of charge carriers (n) in each condition was calculated based on Hall effect,[45] and to analyze the influence of the Fe^{3+}−CA complexation to the SAM−semiconductor interface, they were normalized with respect to CA. In both highly concentrated (10 mM NaCl) and DI water conditions (Figure 10b), the normalized carrier density of the semiconductor was decreased from 1 to 0.96 after the Fe^{3+}−CA complexation. Although n from the Hall effect presents a bulk characteristic of the semiconductor, this n reduction after the Fe^{3+} chemisorption at SAM suggested that the interfacial molecular effect at the ESS structure can be critically influential to the adjoining semiconducting region.[20] These results could provide significant evidence for the electrical behaviors of CA−IIT and Fe−IIT (Figure 8a). Consistently with Figure 8c, the Fe^{3+}−CA complexation at SAM could deplete charge carriers at the SAM−semiconductor interface by its dipole potential shift. This is in accordance with a negative work function shift of CA after binding Fe^{3+} on them (Figure 2d). Hence, $\boldsymbol{R_{sc}}$ can be increased, thereby

escalating the voltage drop effect (the increase of V_p in Figure 8a) at the SAM–semiconductor interface. Although there should be detailed understandings for surficial molecular effect, the Fe^{3+} complexation–induced molecular dipole shift (Figure 2d and Figure 10b) might be resulted from extra–coordinations of negative hydroxide ions in the Fe^{3+}–CA complexes (Figure 7b) at the electrolyte–contacted state. In addition, the weak variation of I_p upon the Fe^{3+} complexation could be induced from this charge carrier depletion effect, which can compete with the increase of surface charges due to the bound hydroxide ions in the Fe^{3+}–CA complexes (Figure 7b).

.

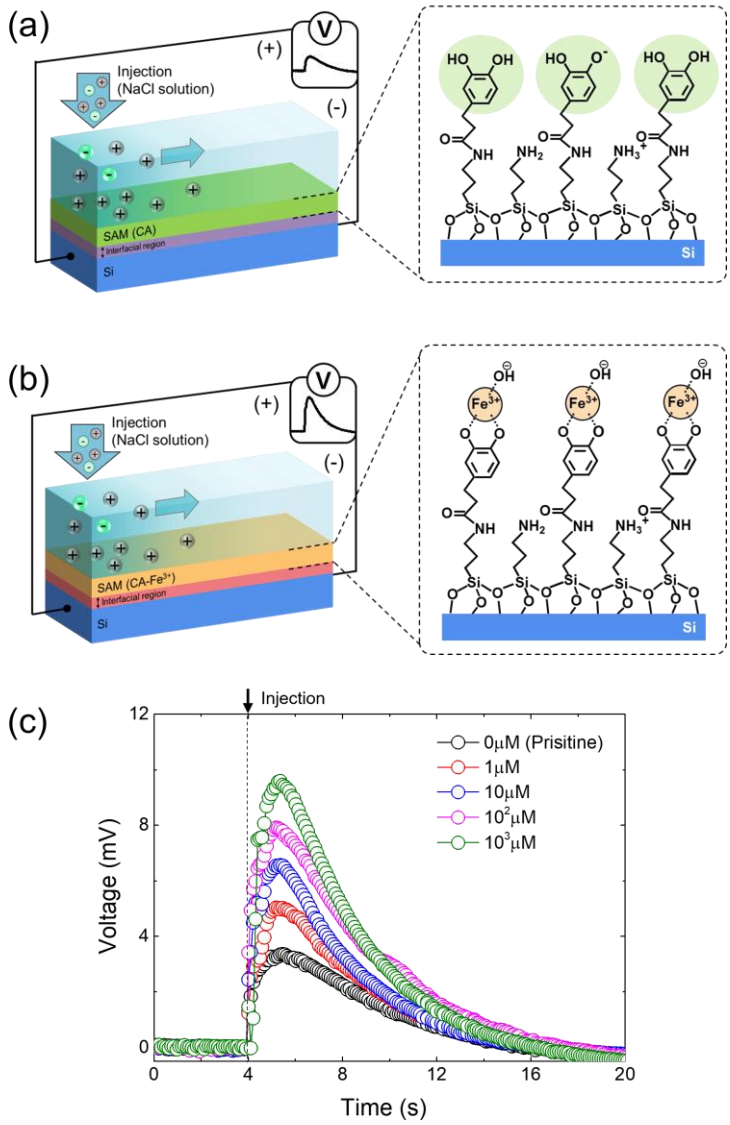

Figure 7. (a,b) A schematic image of interfacial adsorption-induced electric output variation in the catechol group (CA)-modified ionovoltaic device (CA-IIT) and corresponding interfacial illustrations, which display (a) a pristine state (CA) and (b) Fe^{3+} adsorbed CA state (CA-Fe^{3+}). Dashed lines in Figure 7 (b) denotes coordination bonding between Fe^{3+} and O^{-} ligands. (c) Generated voltage as a function of time under different $FeCl_3$ concentrations.

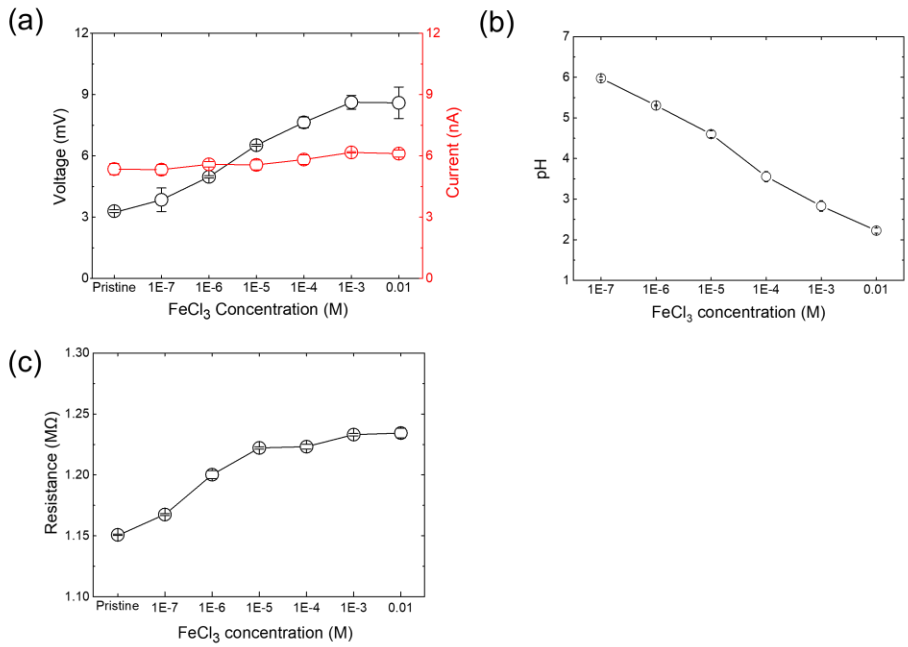

Figure 8. (a) Peak voltage and current as a function of exposed $FeCl_3$ concentrations in the catechol group-modified device (CA-IIT) and Fe^{3+} adsorbed device (Fe-IIT). (b) The pH of $FeCl_3$ solution as a function of concentration. (c) Device resistance as a function of exposed $FeCl_3$ concentrations. Resistances in each condition was obtained from a slope of current-voltage curves, which were measured at both terminals.

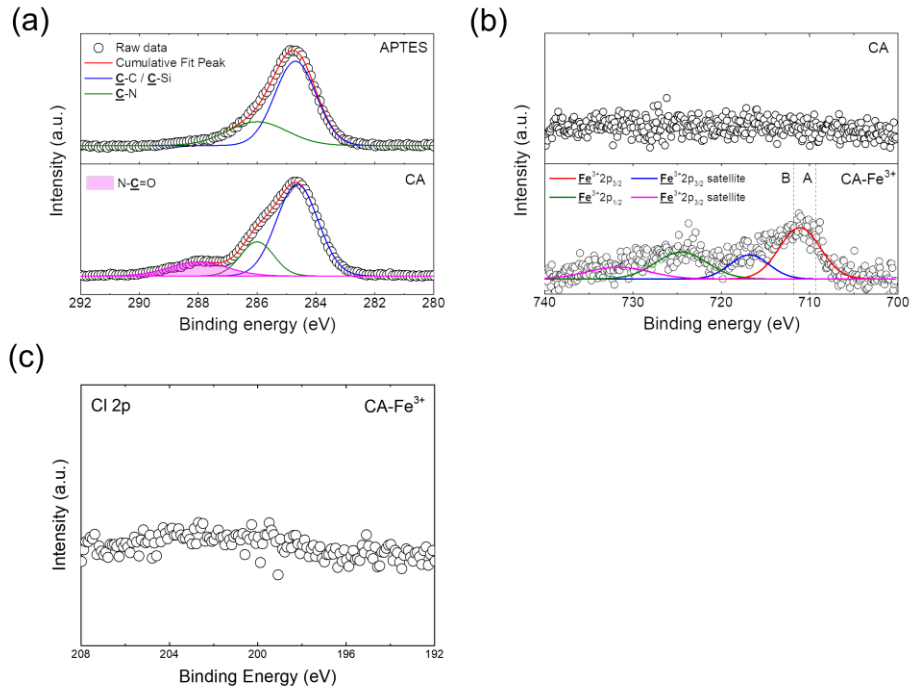

Figure 9. (a) C1s XPS spectra of (top) APTES−modified device and (bottom) catechol (CA)−modified device. (b) Fe2p XPS spectra of (top) a pristine CA and (bottom) Fe^{3+} adsorbed surface (CA−Fe^{3+}) (exposed to 100 μM $FeCl_3$). Dashed lines of A and B denote the peak positions of Fe $2p_{3/2}$ peak obtained from Fe^{2+} with O^- ligands and Fe^{3+} with Cl^- ligands, respectively. (c) Cl 2p XPS spectrum of CA−Fe^{3+} surface (exposed to 100 μM $FeCl_3$).

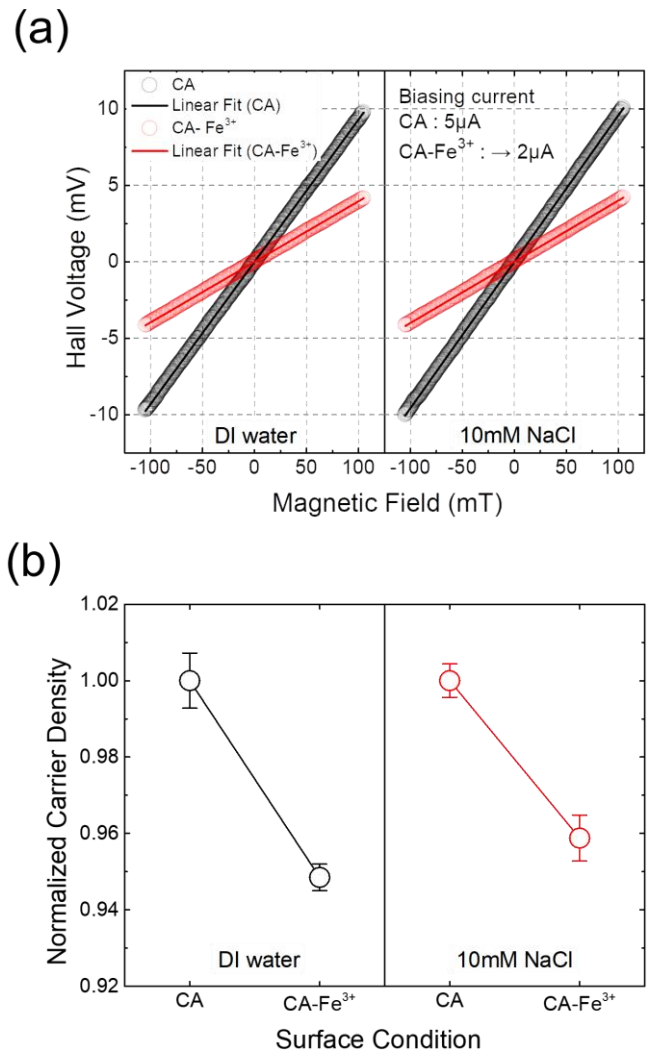

Figure 10. (a) Hall voltage of the semiconducting layer as a function of magnetic field at the ESS interface. Liquid–interfacing Hall measurements were conducted under (left) DI water and (right) 10 mM NaCl conditions. Constant currents of 5 and 2 μA were applied to catechol group–modified device (CA) (black) and Fe^{3+} adsorbed device (CA–Fe^{3+}) (red). Magnetic field was swept from −105 mT to 105 mT. (b) Normalized carrier density as a function of surface states (CA and CA–Fe^{3+}) under different electrolyte conditions ((left) DI water and (right) 10 mM NaCl).

3.3. Applicability as a sensor platform

To further investigate the electrical outputs of IIT depending on the ion−ligand complexation, different metal ions, Fe^{3+}, Al^{3+}, and Cu^{2+} (Cl^- as a same counterion), were exposed to IIT surface (Figure 11). The experiments were conducted in the same method with the $FeCl_3$ test shown in Figure 7, and output voltages depending on each ion concentration were presented as relative peak voltage changes ($(V-V_0)/V_0$, where V_0 is a peak voltage at pristine CA). Interestingly, upon the metal ion exposures, the output voltages from IIT were increased in all cases, but their magnitudes were varied depending on each ion species. From linear regressions of these output voltage changes, slopes of each voltage variations were obtained as follows; Fe^{3+} : 3.155 M^{-1}, Al^{3+} : 0.6196 M^{-1}, Cu^{2+} : 0.1052 M^{-1}. As mentioned in a previous section, Fe^{3+} can form the most stable complex with the CA.[31,32] Hence, this could be consistent with a radical voltage variation shown in Figure 11, even though CA was anchored in the solid surface. Al^{3+} and Cu^{2+} also could form a mono−complex with the catechol group, but its stability constants were much lower than the Fe^{3+}−CA mono−complex (a stability constant order of metal ion−catechol mono−complex; Fe^{3+}>Al^{3+}>Cu^{2+}).[31] In addition to this, an acidity difference between these ions also could contribute to this voltage variation. Especially, the drastic voltage behavior in Fe^{3+} could be attributed to a higher acidity of Fe^{3+}, forming more OH^- bound state, than other ions in aqueous state. As discussed in a previous section, the more OH^- binding to the transition metal ion−CA complex could induce much larger interfacial molecular dipole shift, thereby triggering higher depleting effect at the SAM−semiconductor

interface. Although in-depth understandings are required to the interfacial state of the coordination complex and their interactions within the ESS interface, the voltage behaviors shown in Figure 11 can represent an interesting mutual interaction between the ESS interface depending on influences of transition metal ion-interfacial molecular complexes. Therefore, this result shows that CA-IIT have an applicability as novel ion sensor for specific ferric ion detection by observing significant signal change by adsorption compared to other metal ions.

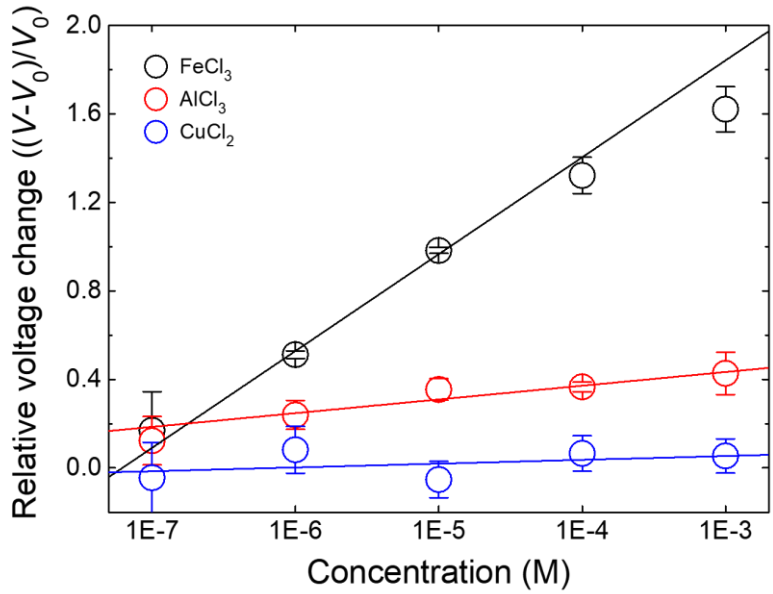

Figure 11. Relative peak voltage changes as a function of metal ion solution concentrations. Here, V_0 denotes a peak voltage at the pristine (CA−modified) state. According to linear fitting, each slope of $FeCl_3$, $AlCl_3$, and $CuCl_2$ are 3.155, 0.6196, and 0.1052 M^{-1}, respectively.

Chapter 4. Conclusion

In summary, the ionovoltaic mechanism at the ESS interface and the corresponding influences of interfacial molecular layer were interrogated *via* the chemical controls of the molecular layer. The ion–charge carrier interplays originated from the interfacial dipole potential was verified in IIT. In addition, influences of interfacial molecular layer to this system were demonstrated *via* the amine group chemistry–based CA modification and the ion–ligand complexation therein. Both IIT and the liquid–interfacing Hall measurement consistently proved that the Fe^{3+}–CA complexation at the electrolyte–semiconductor interface can deplete the charge carrier density at the semiconducting layer adjacent to the interface, thereby the suggesting an impact of surficial molecular layer to an energy level of charge carriers under the electrolyte–interfacing condition. These results indicated that the concept of this IIT could be applicable to analyzing the electrolyte–semiconductor interface, which is difficult to observe with conventional analytic techniques. In addition, with diverse surface functionalization chemistry, this ion dynamics–driven transducing system could be utilized as effective interfacial or molecular probing devices.

Bibliography

[1] V. R. Stamenkovic, D. Strmcnik, P. P. Lopes, N. M. Markovic, *Nat. Mater.* **2016**, *16*, 57.

[2] C. Leighton, *Nat. Mater.* **2019**, *18*, 13.

[3] J. Yin, X. Li, J. Yu, Z. Zhang, J. Zhou, W. Guo, *Nat. Nanotechnol.* **2014**, *9*, 378.

[4] K. Wang, J. Li, *J. Mater. Chem. A* **2021**, *9*, 8870.

[5] J. Yin, Z. Zhang, X. Li, J. Yu, J. Zhou, Y. Chen, W. Guo, *Nat. Commun.* **2014**, *5*, 3582.

[6] W. Fei, C. Shen, S. Zhang, H. Chen, L. Li, W. Guo, *Nano Energy* **2019**, *60*, 656.

[7] H. Jin, S. G. Yoon, W. H. Lee, Y. H. Cho, J. Han, J. Park, Y. S. Kim, *Energy Environ. Sci.* **2020**, *13*, 3432.

[8] T. G. Yun, J. Bae, A. Rothschild, I.-D. Kim, *ACS Nano* **2019**, *13*, 12703.

[9] J. Park, S. Song, Y. Yang, S. H. Kwon, E. Sim, Y. S. Kim, *J. Am. Chem. Soc.* **2017**, *139*, 10968.

[10] H. Ryu, J. H. Lee, U. Khan, S. S. Kwak, R. Hinchet, S.-W. Kim, *Energy Environ. Sci.* **2018**, *11*, 2057.

[11] A. T. Liu, G. Zhang, A. L. Cottrill, Y. Kunai, A. Kaplan, P. Liu, V. B. Koman, M. S. Strano, *Adv. Energy Mater.* **2018**, *8*, 1802212.

[12] J. Park, S. Song, C. H. Shin, Y. J. Yang, S. A. L. Weber, E. Sim, Y. S. Kim, *Angew. Chemie – Int. Ed.* **2018**, *57*, 2091.

[13] Y. J. Yang, J. Park, S. G. Yoon, Y. S. Kim, *Nano Energy* **2017**, *40*, 447.

[14] Y. J. Yang, S. G. Yoon, C. H. Shin, H. Jin, W. H. Lee, J. Park, Y. S. Kim, *Nano Energy* **2019**, *57*, 195.

[15] J. Park, Y. J. Yang, S. H. Kwon, S. G. Yoon, Y. S. Kim, *Nano Energy* 2017, *42*, 257.

[16] S. G. Yoon, Y. Yang, H. Jin, W. H. Lee, A. Sohn, S. Kim, J. Park, Y. S. Kim, *Adv. Mater.* 2019, *31*, 1806268.

[17] S. G. Yoon, B. J. Park, H. Jin, W. H. Lee, J. Han, Y. H. Cho, H. Yook, J. W. Han, Y. S. Kim, *Small Methods* 2021, *5*, 2100323.

[18] S. G. Yoon, Y. J. Yang, J. Yoo, H. Jin, W. H. Lee, J. Park, Y. S. Kim, *ACS Appl. Electron. Mater.* 2019, *1*, 1746.

[19] S. G. Yoon, H. Jin, W. H. Lee, J. Han, Y. H. Cho, Y. S. Kim, *Nano Energy* 2021, *80*, 105522.

[20] W. H. Lee, S. G. Yoon, H. Jin, J. Yoo, J. Han, Y. H. Cho, Y. S. Kim, *Adv. Mater.* 2021, *33*, 2007581.

[21] Z. Zhang, J. T. Yates, *Chem. Rev.* 2012, *112*, 5520.

[22] A. Vilan, D. Cahen, *Chem. Rev.* 2017, *117*, 4624.

[23] J. Nie, Z. Ren, L. Xu, S. Lin, F. Zhan, X. Chen, Z. L. Wang, *Adv. Mater.* 2020, *32*, 1905696.

[24] D. J. Ellison, B. Lee, V. Podzorov, C. D. Frisbie, *Adv. Mater.* 2011, *23*, 502.

[25] E. Metwalli, D. Haines, O. Becker, S. Conzone, C. G. Pantano, *J. Colloid Interface Sci.* 2006, *298*, 825.

[26] Y. Ofir, N. Zenou, I. Goykhman, S. Yitzchaik, *J. Phys. Chem. B* 2006, *110*, 8002.

[27] C. H. Kuo, C. P. Liu, S. H. Lee, H. Y. Chang, W. C. Lin, Y. W. You, H. Y. Liao, J. J. Shyue, *Phys. Chem. Chem. Phys.* 2011, *13*, 15122.

[28] T. J. B. W. M. Haynes, David R. Lide, *CRC Handbook of Chemistry and Physics, CRC press*, Florida, USA 2016.

[29] M. Z. Bazant, K. Thornton, A. Ajdari, *Phys. Rev. E – Stat. Physics, Plasmas, Fluids, Relat. Interdiscip. Top.* 2004, *70*, 24.

[30] Robert F. Pierret, *Semiconductor Device Fundamentals*, Pearson Education, India 1996.

[31] A. E. Martell, R. M. Smith, *Other Organic Ligands*, Springer Science+Business Media, New York, USA 1977.

[32] M. J. Sever, J. J. Wilker, *J. Chem. Soc. Dalt. Trans.* 2004, *4*, 1061.

[33] J. Lee, J. Ko, J. Ryu, J. Shin, H. Kim, D. Sohn, *Colloids Surfaces A Physicochem. Eng. Asp.* 2016, *511*, 55.

[34] N. Holten-Andersen, M. J. Harrington, H. Birkedal, B. P. Lee, P. B. Messersmith, K. Y. C. Lee, J. H. Waite, *Proc. Natl. Acad. Sci. U. S. A.* 2011, *108*, 2651.

[35] H. Zeng, D. S. Hwang, J. N. Israelachvili, J. H. Waite, *Proc. Natl. Acad. Sci. U. S. A.* 2010, *107*, 12850.

[36] Q. Liu, X. Lu, L. Li, H. Zhang, G. Liu, H. Zhong, H. Zeng, *J. Phys. Chem. C* 2016, *120*, 21670.

[37] B. Niu, K. Xiao, X. Huang, Z. Zhang, X. Y. Kong, Z. Wang, L. Wen, L. Jiang, *ACS Appl. Mater. Interfaces* 2018, *10*, 22632.

[38] A. Manakhov, J. Čechal, M. Michlíček, D. V. Shtansky, *Appl. Surf. Sci.* 2017, *414*, 390.

[39] T. Yamashita, P. Hayes, *Appl. Surf. Sci.* 2008, *254*, 2441.

[40] A. P. Grosvenor, B. A. Kobe, M. C. Biesinger, N. S. McIntyre, *Surf. Interface Anal.* 2004, *36*, 1564.

[41] M. D. Lind, *J. Chem. Phys.* 1967, *47*, 990.

[42] S. A. Cotton, *J. Coord. Chem.* 2018, *71*, 3415.

[43] G. A. Lawrance, *Introduction to Coordination Chemistry*, John Wiley & Sons, UK 2013.

[44] F. P. Adamson AW, *Concepts of Inorganic Photochemistry*, Wiley, 1975.

[45] E. H. Hall, Am. J. Math, *Nature* 1879, *2*, 287.

Abstract in Korean

이온-고체 표면 간의 상호 작용은 다양한 전기 화학 시스템이나 전해질 기반의 에너지 변환 장치와 같은 액체 계면을 지닌 장치의 기본 원리 중 하나이다. 특히 전하 운반체를 지닌 고체 표면으로 형성된 계면에서의 상호 작용은 이러한 장치들의 작동에 있어 중추적인 역할을 하지만, 각 효과들에 대한 세세한 이해와 해석은 여전히 미지의 영역으로 남아 있다. 이 논문에서는 이온 동역학적 발전 기반의 에너지 변환장치(이온발전소자)의 구조 중 계면에 존재하는 자기조립분자들을 조절하여 전해질-반도체 계면에서의 이온과 전하 운반체 간의 상호 작용에 대한 연구가 진행되었다. 계면에서의 이온 확산으로 인한 전기 신호 생성 메커니즘은 자기조립물질들의 쌍극자 전위 효과에서 비롯된 이온-전하 운반체 간의 상호 작용의 관점에서 설명되었다. 또한, 이러한 효과는 계면에 존재하는 분자층의 화학적 기능화와 표면의 리간드와 금속 이온의 화합물 형성을 통해 조절되는 것으로 밝혀졌다. 표면 분석 기술과 액체와 계면을 형성한 소자에서의 홀효과 측정을 통해, 이온-리간드 복합체 형성의 정도에 따른 이온발전소자의 전기적 신호 변화를 전해질-자기조립분자층-반도체 구조의 계면에서 이루어지는 이온-전하 운반체의 상호 작용의 관점으로 해석하였다. 그리고 이런 이온 확산 기반의 이온발전소자에서 발생한 전기적 신호 변화를 통해 전기이중층 내의 일시적인 이온 거동과 상호작용하는 자기조립분자물질들이 인접한 반도체층에 영향을 끼치는 것을 증명해낼 수 있다. 결과적으로, 이 시스템은 계면 영역에서 발생하는 화학적 및 물리적 영향을 포함한 분자 상호 작용을 연구하는 데 적용될 수 있다.